

Detection of internal fields in double-metal terahertz resonators

Oleg Mitrofanov, Zhanghua Han, Fei Ding, Sergey I. Bozhevolnyi, Igal Brener, and John L. Reno

Citation: *Appl. Phys. Lett.* **110**, 061109 (2017); doi: 10.1063/1.4975802

View online: <http://dx.doi.org/10.1063/1.4975802>

View Table of Contents: <http://aip.scitation.org/toc/apl/110/6>

Published by the [American Institute of Physics](#)

Articles you may be interested in

[Terahertz plasmonic rectification in a spatially periodic graphene](#)

Applied Physics Letters **110**, 061106 (2017); 10.1063/1.4975829

[Optically thin hybrid cavity for terahertz photo-conductive detectors](#)

Applied Physics Letters **110**, 041105 (2017); 10.1063/1.4974482

[Controlling the optical spin Hall effect with light](#)

Applied Physics Letters **110**, 061108 (2017); 10.1063/1.4975681

[Strong coupling between Tamm plasmon polariton and two dimensional semiconductor excitons](#)

Applied Physics Letters **110**, 051101 (2017); 10.1063/1.4974901

[Magnetic field sensor based on coupled photonic crystal nanobeam cavities](#)

Applied Physics Letters **110**, 061110 (2017); 10.1063/1.4975804

[Sensing with toroidal metamaterial](#)

Applied Physics Letters **110**, 121108 (2017); 10.1063/1.4978672



www.trekinc.com



**HIGH-VOLTAGE AMPLIFIERS AND
ELECTROSTATIC VOLTMETERS**

ENABLING RESEARCH AND
INNOVATION IN DIELECTRICS,
MICROFLUIDICS,
MATERIALS, PLASMAS AND PIEZOS

Detection of internal fields in double-metal terahertz resonators

Oleg Mitrofanov,^{1,2,a)} Zhanghua Han,^{3,a)} Fei Ding,⁴ Sergey I. Bozhevolnyi,⁴ Igal Brener,^{2,5} and John L. Reno^{2,5}

¹University College London, Electronic and Electrical Engineering, London WC1E 7JE, United Kingdom

²Center for Integrated Nanotechnologies, Sandia National Laboratories, Albuquerque, New Mexico 87185, USA

³Centre for Terahertz Research, China Jiliang University, Hangzhou 310018, China

⁴Centre for Nano Optics, University of Southern Denmark, Odense 5230, Denmark

⁵Sandia National Laboratories, Albuquerque, New Mexico 87185, USA

(Received 8 November 2016; accepted 26 January 2017; published online 10 February 2017)

Terahertz (THz) double-metal plasmonic resonators enable enhanced light-matter coupling by exploiting strong field confinement. The double-metal design however restricts access to the internal fields. We propose and demonstrate a method for spatial mapping and spectroscopic analysis of the internal electromagnetic fields in double-metal plasmonic resonators. We use the concept of image charges and aperture-type scanning near-field THz time-domain microscopy to probe the fields confined within the closed resonator. The experimental method opens doors to studies of light-matter coupling in deeply sub-wavelength volumes at THz frequencies. *Published by AIP Publishing.* [<http://dx.doi.org/10.1063/1.4975802>]

In semiconductors, strong light-matter coupling leads to intriguing quantum phenomena^{1–3} and non-linear optical effects,⁴ which can be exploited in photonic devices.⁵ The interaction of excitons with photons of an optical cavity, for instance, produces exciton-polaritons, a superposition of the photon and exciton states, manifested in a splitting of the exciton energy level, which enables the concept of polariton laser.^{6,7} In the terahertz (THz) frequency range, the light-matter interaction can reach the ultrastrong coupling regime,⁸ in which even more unusual quantum effects are predicted.^{9–11}

One promising approach for enhancing light-matter coupling at THz frequencies is to confine the THz fields to a sub-wavelength volume using broadband or resonant plasmonic structures.^{12–16} Several resonator designs have been proposed recently.^{12–14,16–18} A high degree of field confinement however limits possibilities for investigating single resonators. Instead, THz light-matter coupling effects are studied using arrays of identical resonators, which can introduce inhomogeneous broadening and inter-resonator coupling. To reduce the number of resonators, complementary structures have been proposed.¹⁶ Yet, studies of THz light-matter coupling in a single sub-wavelength resonator using far-field spectroscopy remain challenging. Furthermore, the far-field analysis lacks the spatial field distribution information and can also display spectral shifts.¹⁹

To enable investigations of light-matter coupling effects within a stand-alone double-metal resonator in the THz frequency range, here, we propose and demonstrate the use of aperture-type near-field microscopy. Using the concept of image charges, we map the spatial distribution of the internal resonator fields, directly probe their frequency spectrum, and investigate the field dynamics on a picosecond time scale.

Double-metal resonators consist of two isolated metallic structures separated by a thin semiconductor layer. They

enable efficient energy coupling from a THz wave to a small volume, which can contain a nano-scale electronic system, such as quantum wells or quantum dots. The double-metal geometry ensures strong and adjustable field enhancement with a well-defined polarization of the THz field, often required to fulfill selection rules of optical transitions.

To access the electromagnetic fields inside the double-metal resonator, we exploit the mirror symmetry of the structure [Fig. 1(a)]. A planar resonator is positioned above a metallic surface serving as a mirror plane and forming a double-metal resonator, in which the bottom half is replaced

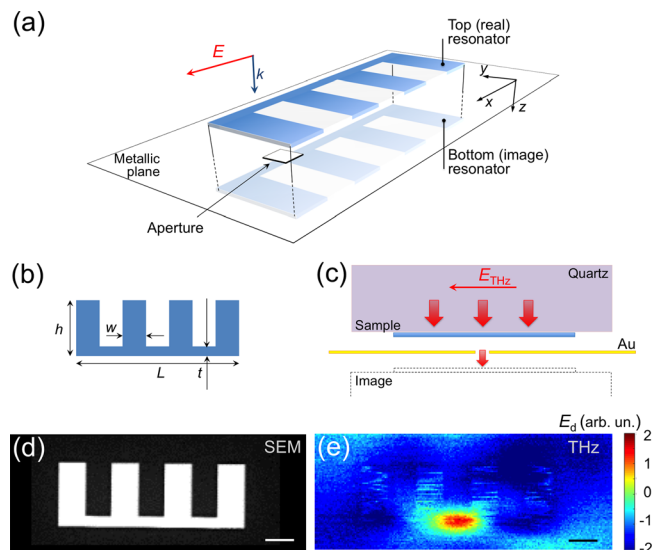


FIG. 1. (a) Schematic diagram of the double-metal resonator formed by a planar resonator and its mirror image. (b) Resonator design (xy -plane). (c) Side view (xz -plane) of the experimental configuration: the gold plane (Au) of the probe forms an image resonator below the sample; the electric field coupled through the aperture is determined by the field inside the double-metal resonator. (d) Scanning electron microscope image of the resonator structure and (e) an experimental THz field map ~ 2 ps after excitation by a THz pulse. The scale bars in (d) and (e) are $20 \mu\text{m}$.

^{a)} Authors to whom correspondence should be addressed. Electronic addresses: o.mitrofanov@ucl.ac.uk and han@cjl.u.edu.cn

by an image of the top resonator, i.e., the normal field $E_z(x,y)$ within the mirror plane is equivalent to the field inside the double-metal resonator. This field can be mapped experimentally using a sub-wavelength aperture in the mirror. The aperture admits only a small fraction of the resonator energy below the mirror plane, where we detect it by a photoconductive THz antenna placed within 300 nm from the aperture.²⁰ The aperture size was chosen to be $5 \times 5 \mu\text{m}^2$, small in comparison with the wavelength and the size of the resonator.

A spoof surface plasmon resonator was chosen for the top resonator geometry.²¹ It supports a series of plasmonic modes determined by the number of periods (grooves) in the resonator [Fig. 1(b)]. These modes were investigated numerically in Ref. 22. It was found that the surface plasmon wavevector k_m in this structure is larger than the free space wavevector due to the fins. Oriented perpendicular to the length of the resonator, the fins provide additional path for the surface plasmon waves, and, as a result, the wavevector is determined by the combined lengths of the base L and the fins h , rather than the base alone. A similar increase in the surface plasmon wavevector is found in corrugated waveguides (spoof plasmons). The resonance condition can be defined²² as $k_m L + \Phi = m\pi$, ($m = 1, 2, 3, \dots$), where m is an integer, indicating the resonance order and Φ is the phase shift on reflection from the resonator ends. The first three resonances correspond to $m = 1, 2$, and 3 and are referred to as $\lambda/2$, λ , and $3/2\lambda$ resonances here. Due to symmetry, only resonances corresponding to odd m can be excited by a linearly polarized incident wave at normal incidence. The $\lambda/2$ and $3/2\lambda$ modes were predicted to exhibit relatively narrow THz resonances.²²

When a metallic surface is introduced parallel to the resonator surface, a double-metal resonator is formed. It supports plasmonic modes confined between the top (real) and bottom (image) resonators [Fig. 1(c)]. First, we investigated a simple double-metal resonator filled with air. Dimensions of the resonator, $L = 140 \mu\text{m}$, $h = 50 \mu\text{m}$, $w = 20 \mu\text{m}$, and $t = 8 \mu\text{m}$, were selected to produce fundamental resonances at 0.5 and 1 THz.

Samples were fabricated by electron-beam lithography and thermal evaporation of a 200 nm thick Au layer on a 0.5 mm thick quartz substrate [Fig. 1(d)]. The resonator was excited at normal incidence from the substrate side using a short THz pulse generated in a ZnTe crystal by 100 fs optical pulses with the central wavelength of $\sim 800 \text{ nm}$.²³ The THz beam was polarized along the x -axis, and it had an approximate diameter of $500 \mu\text{m}$.

Surface waves excited at the resonator edges by the THz pulse are guided between the resonator and the metallic surface.²⁴ Upon reflection from the opposite edges, standing surface waves are formed within the resonator. These standing surface waves represent the fundamental modes of the resonator.²⁵ A corresponding field distribution is mapped point by point by scanning the aperture within the mirror plane at $\sim 1 \mu\text{m}$ from the resonator surface.

The field distribution detected inside the resonator approximately 2 ps after excitation is shown in Fig. 1(e). The field map reflects the resonator geometry and shows the strongest signal at the center of the narrow ($8 \mu\text{m}$ wide)

horizontal bar (resonator base). In this region, the E_z component of electric field dominates due to the boundary conditions ($E_x = E_y = 0$) imposed by the metallic surfaces. The field coupled through the aperture in this case is proportional to dE_z/dx .^{24,26} The observed symmetric pattern corresponds to the anti-symmetric E_z field distribution of the resonator bright modes. To quantify the field enhancement in the resonator, time-domain waveforms of the THz field were recorded at two principal points: between the central resonator fins (Point A) and at the field maximum (Point B) [Fig. 2(a)]. In Point A, the waveform shows the incident THz pulse and its replica arriving 7–8 ps later. The replica is due to the incident pulse partially reflected from the sample surfaces; after travelling within the 0.5 mm substrate backward and forward, the reflected pulse reaches the detector ~ 7 ps after the main pulse. The Fourier transform of the waveform shows corresponding Fabry-Perot resonances occurring with a period of $\sim 145 \text{ GHz}$ (Fig. 2(b)). We found that the effect of the resonator on the detected field was negligible when the aperture is positioned between the central fins. The spectrum of the field at Point A, therefore, is used as the reference. The spectrum of the incident pulse measured without the sample is also shown in Fig. 2(b) for comparison (black line).

The time-domain waveform and the spectrum of the field recorded at Point B are strikingly different: the waveform contains periodic oscillations, and the Fourier transform shows enhanced field amplitudes at two relatively narrow frequency bands: 0.5 and 1 THz. The field enhancement E_B/E_A is shown in the inset of Fig. 2(b): the amplitude is enhanced by over 20 times at 0.5 THz, whereas a weaker enhancement (~ 6 times) is observed at 1 THz. It was shown numerically that the $3/2\lambda$ resonance for this resonator design

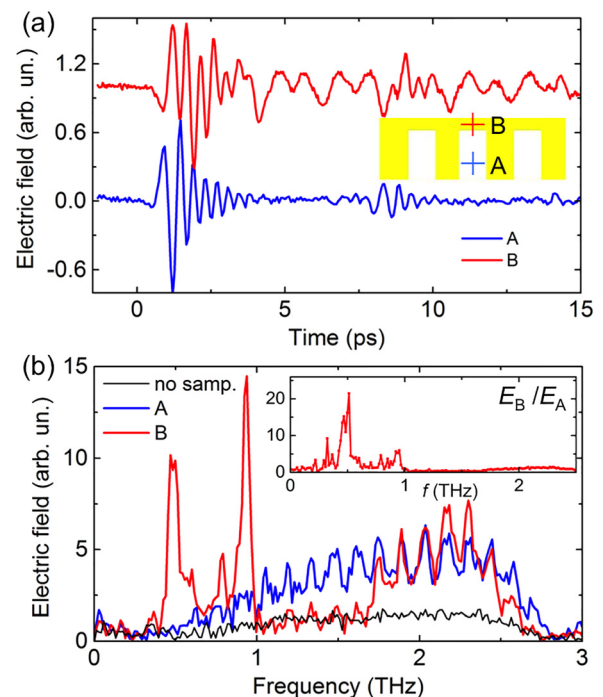


FIG. 2. Near-field waveforms (a) and spectra (b) detected between the central resonator fins (Point A) and at the center of the horizontal bar (Point B). The black line shows the spectrum of the incident pulse. The inset shows the spectral amplitude ratio E_B/E_A at Points B and A.

occurs at approximately twice the frequency of the $\lambda/2$ resonance.²² This is due to the strong dispersion of spoof plasmons near the frequency of the $3/2\lambda$ resonance.²² Our experimental results show that the second resonant in this structure also occurs at approximately twice the frequency of the first resonance, indicating that the observed resonance correspond to the $\lambda/2$ and $3/2\lambda$ modes. We will show later that the phase map of the detected field confirms this. The resonances are followed by a band of suppressed field, between 1.05 and 1.8 THz, after which the spectral amplitude recovers to the incident field amplitude level.

The suppression of the field within this band is due to dispersion of spoof plasmons. We note that the three grooves in this resonator design naturally support the $3/2\lambda$ resonance.²² The $3/2\lambda$ resonance can also be viewed as the constructive interference of spoof plasmons travelling within the periodic structure of the resonator. At the resonance frequency, the vector of the spoof plasmons k_3 is matched to the resonator periodicity. Above the frequency of the $3/2\lambda$ resonance, however, the spoof plasmons experience destructive interference within the structure, similar to the destructive interference that leads to the formation of forbidden bands in dispersion of corrugated waveguides.²⁷ In-depth analysis of the field suppression in the band above the $3/2\lambda$ resonance frequency and its relationship to dispersion of spoof plasmon modes will be discussed elsewhere.

To determine the optimal aperture location for probing the internal fields, we recorded full time-domain waveforms along a line passing through the bar center parallel to the y -axis [Fig. 3(a)]. A space-time map of the field $E(t,y)$ shows that the resonant oscillations lasting over 25 ps are localized within the horizontal bar. The corresponding Fourier map $E(f,y)$ shows that the oscillations contain the two resonances at 0.5 THz and 1 THz. Figure 3(b) displays the Fourier maps $E(f,y)$ normalized to the spectrum of the THz wave transmitted through the substrate $E(f,y=40\mu\text{m})$ in the spectral

regions near the two resonances. The enhanced field is confined to the area of the resonator base with no enhancement away from the metal area.

To investigate the nature of resonances, we recorded the temporal field evolution along the resonator base, as shown in the inset of Fig. 3(c). We found that the 0.5 THz mode is uniformly distributed along the base with a constant phase within the base area [Fig. 3(c), left panel], whereas the phase for the field at 1 THz alternates between $-\pi/2$ and $\pi/2$ relative to the incident field [Fig. 3(c), right panel]. These phase maps are consistent with the $\lambda/2$ and $3/2\lambda$ modes of the double-metal plasmonic resonator. The inset of Fig. 3(c) illustrates schematically the charge distribution for the $\lambda/2$ and $3/2\lambda$ resonances.

Finally, we investigated resonators containing an internal GaAs layer. A single-metal resonator was sandwiched between a 0.5 mm thick sapphire substrate and a $1.5\mu\text{m}$ thick GaAs layer as illustrated schematically in Fig. 4(a). The resonator was bonded to sapphire by a layer of epoxy ($\sim 5\mu\text{m}$), and GaAs was thinned by lapping and chemical etching to keep only a $1.5\mu\text{m}$ thick layer of GaAs. When placed parallel to a metallic surface of the near-field probe, this structure is equivalent to a double-metal plasmonic resonator with a $3\mu\text{m}$ thick GaAs layer.

To keep the resonances within the range of our measurement system (0.4–2.5 THz), two scaled-down resonator designs were fabricated: MDM-A with $L = 35\mu\text{m}$, $h = 11\mu\text{m}$, and $w = 5\mu\text{m}$ and MDM-B with $L = 21\mu\text{m}$, $h = 7\mu\text{m}$, and $w = 3\mu\text{m}$ [Fig. 1(b)]. The horizontal base width t , where the resonant fields are localized, was kept $2\mu\text{m}$ in both cases.

The THz field at the center of the resonator base was measured for the GaAs surface practically in contact with the metallic surface and for a range of air gaps between them. Similarly to the enhancement observed in the air-filled resonator, resonant THz fields were observed at the base center of the MDM structures. THz near-field spectra normalized to the

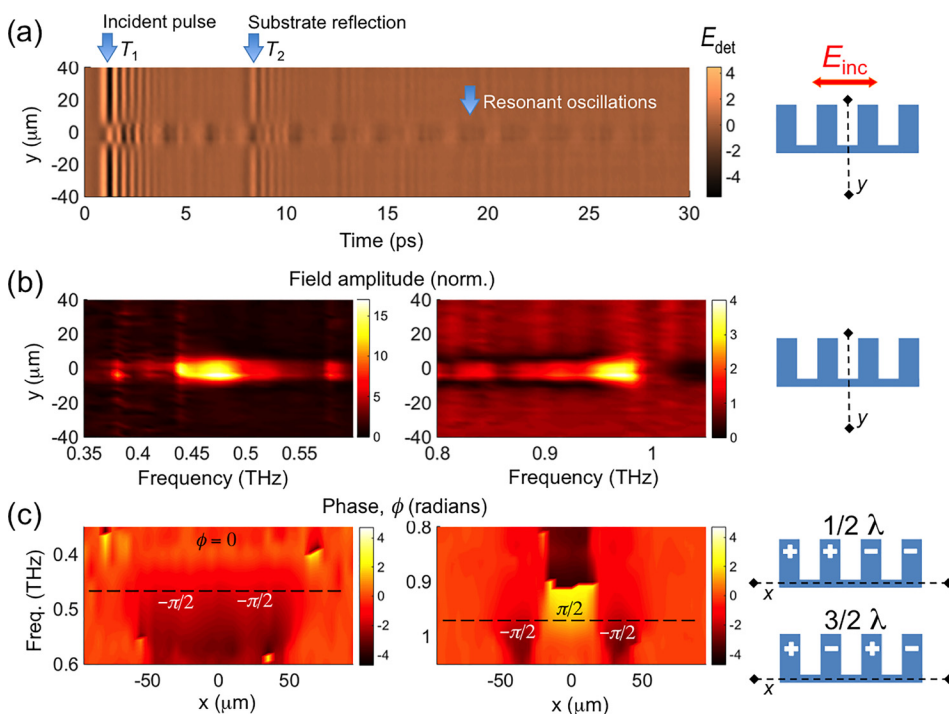


FIG. 3. (a) Near-field space-time map measured along the y -axis (inset). The arrows indicate the incident THz pulse (T_1), the first reflection within the substrate (T_2) and the resonant oscillations within the resonator. The inset shows the spatial position of the line scan (dashed line). (b) Field enhancement maps near the two resonance frequencies, 0.5 and 1 THz. (c) Phase maps of the field along the horizontal base of the resonator. The dashed lines indicate the resonance frequencies (0.5 and 1 THz). The inset shows the spatial position of the line scan (dashed line) and the charge distribution for the $\lambda/2$ and $3/2\lambda$ resonances.

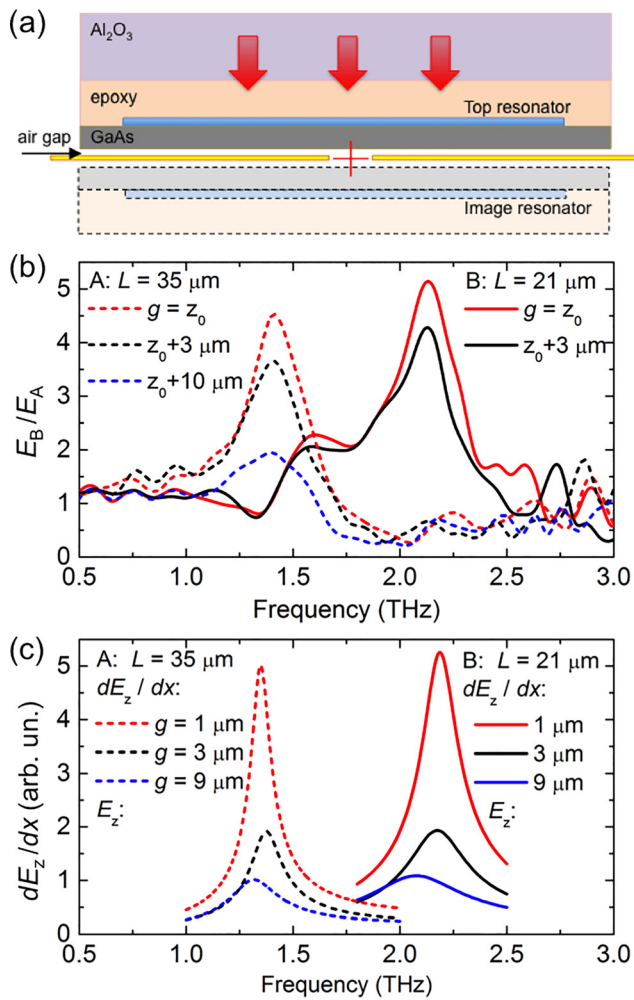


FIG. 4. (a) Schematic side view (xz -plane) diagram of the experimental configuration for probing the internal fields of the MDM resonators. Experimental (b) and simulated (c) normalized spectra of the field at Point B for resonators with $L = 21 \mu\text{m}$ and $35 \mu\text{m}$ and the air gap ranging between $g = 1\text{--}10 \mu\text{m}$.

field detected for a similar structure without the resonator show clear enhancement peaks at 1.4 and 2.1 THz for MDM-A and MDM-B, respectively [Fig. 4(b)]. Numerical simulations confirmed that these resonances are the fundamental dipolar modes.²⁸ To illustrate the agreement with the experimental results, Fig. 4(c) displays numerically simulated spectra of the detected quantity dE_z/dx at Point B. The resonance frequencies for both structures are in good agreement. The experimental spectra show broader resonator line widths. We note that the simulations did not include losses within the epoxy. Absorption in the epoxy can introduce the resonance broadening.

A small air gap between the GaAs layer and the metallic screen allows us to tune the field enhancement. Figures 4(b) and 4(c) show numerical and experimental spectra for gaps ranging between 1 and 10 μm . The field enhancement increases strongly for smaller gaps. The resonant frequency on the other hand remains within the resonance bandwidth: the MDM-B peak is red-shifted by less than 0.05 THz as the gap increases. MDM-A exhibits a more complex behavior showing a small blue shift first followed by a red shift. The resonance shift to lower frequencies can be explained by the lateral field spreading, which occurs for larger gaps.¹⁷ The shift to higher

frequencies can be attributed to a lower effective dielectric constant ($\epsilon_{\text{air}} < \epsilon < \epsilon_{\text{GaAs}}$) within the volume of the resonator with a larger gap. The balance of these effects keeps the frequency shift relatively small for the considered resonator design. It must be noted that other resonators can produce larger frequency shifts,^{23,25,29} which can be exploited for frequency tuning of the resonances.

Experimentally, we observed the field enhancement of ~ 5 for MDM resonators. It is smaller than the enhancement that we observed for the air filled resonator (~ 20). We attribute the smaller enhancement to the geometry of the MDM structure, which is smaller than the air-filled resonator. In particular, the width of the base in the larger air-filled resonator was $8 \mu\text{m}$, wider than the aperture of the near-field probe. The base width in the MDM structures on the other hand was only $2 \mu\text{m}$, narrower than the aperture. Since the near-field probe collects the THz field over the entire aperture area and the enhanced field is concentrated within the $2 \mu\text{m}$ wide base, the experimentally measured value of field enhancement is lower. We note, however, that the field enhancement for the resonator filled with GaAs is expected to be stronger than that for the resonator filled only with air. The relative ratio E_z/E_0 in Fig. 5(d) reaches the value of >40 , while the enhancement is ~ 20 for a structure filled with air. We expect that near-field probes with smaller input apertures²⁰ could provide quantitative evaluation of the field enhancement for the MDM resonators.

To verify that the spectrum of the experimentally detected field at Point B represents the internal field at the field maximum (Point C), we numerically simulated the field distribution inside the MDM-B using the finite element method.²⁶ Figures 5(a)–5(c) show maps of the E_z component and its derivative dE_z/dx at the resonance frequency (2.19 THz). The spectrum of dE_z/dx at Point B and the spectrum of E_z at the location of the field maximum for the dipolar resonance (Point C) are practically identical [Fig. 5(d)].

In the context of light-matter coupling investigations, these results demonstrate that light-matter interaction phenomena can be studied at THz frequencies in a sub-wavelength volume of a double-metal resonator, avoiding inhomogeneous broadening or inter-resonator coupling occurring in arrays of resonators. The THz field detected by the aperture-type

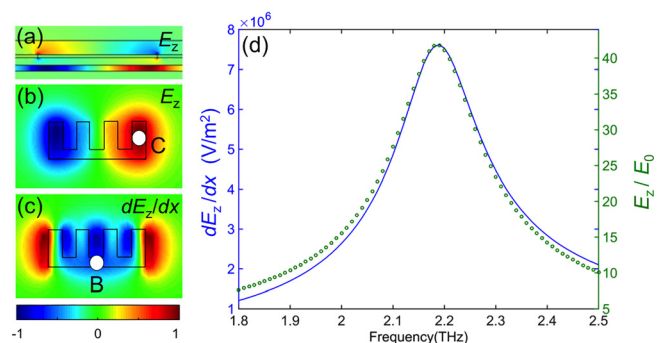


FIG. 5. Numerically simulated spatial distribution of the electric field at the resonance frequency of 2.19 THz for $g = 1 \mu\text{m}$. The maps show the normalized E_z component in the xz -plane (a) and in the xy -plane (b); and its spatial derivative dE_z/dx (c) at the center of the air layer. (d) Spectra of the E_z component (green, circles) and its spatial derivative dE_z/dx (blue) at Points C and B, respectively.

near-field probe (at Point B) represents the E_z component of the field inside the double-metal resonator (point C). Furthermore, control of the air gap enables tuning of the field enhancement. The resonator design considered here exhibits a negligible resonance shift for air gaps $g < 5 \mu\text{m}$. Other designs may have significant frequency shifts and enable resonance frequency tuning.

This work was supported in part by the Royal Society under Grant No. U130493. The experimental work was performed, in part, at the Center for Integrated Nanotechnologies, a U.S. Department of Energy, Office of Basic Energy Sciences user facility. Sandia National Laboratories is a multi-program laboratory managed and operated by Sandia Corporation, a wholly owned subsidiary of Lockheed Martin Corporation, for the U.S. Department of Energy's National Nuclear Security Administration under contract DE-AC04-94AL85000. Z.H. acknowledges the support from National Science Foundation of China (No. 51511140421).

- ¹A. Amo, J. Lefrère, S. Pigeon, C. Adrados, C. Ciuti, I. Carusotto, R. Houdré, E. Giacobino, and A. Bramati, *Nat. Phys.* **5**, 805–810 (2009).
- ²K. G. Lagoudakis, M. Wouters, M. Richard, A. Baas, I. Carusotto, R. André, L. S. Dang, and B. Deveaud-Plédran, *Nat. Phys.* **4**, 706–710 (2008).
- ³I. Carusotto and C. Ciuti, *Rev. Mod. Phys.* **85**, 299–366 (2013).
- ⁴Y. Fu, M. Willander, E. L. Ivchenko, and A. A. Kiselev, *Phys. Rev. B* **55**, 9872 (1997).
- ⁵T. Byrnes, N. Y. Kim, and Y. Yamamoto, *Nat. Phys.* **10**, 803–813 (2014).
- ⁶D. Sanvitto and S. Keňa-Cohen, *Nature Mat.* **15**, 1061–1073 (2016).
- ⁷P. Bhattacharya, T. Frost, S. Deshpande, M. Z. Baten, A. Hazari, and A. Das, *Phys. Rev. Lett.* **112**, 236802 (2014).
- ⁸C. Ciuti, G. Bastard, and I. Carusotto, *Phys. Rev. B* **72**, 115303 (2005).
- ⁹A. Ridolfo, M. Leib, S. Savasta, and M. J. Hartmann, *Phys. Rev. Lett.* **109**, 193602 (2012).

- ¹⁰R. Stassi, A. Ridolfo, O. Di Stefano, M. J. Hartmann, and S. Savasta, *Phys. Rev. Lett.* **110**, 243601 (2013).
- ¹¹S. De Liberato, *Phys. Rev. Lett.* **112**, 016401 (2014).
- ¹²Y. Todorov, A. M. Andrews, I. Sagnes, R. Colombelli, P. Klang, G. Strasser, and C. Sirtori, *Phys. Rev. Lett.* **102**, 186402 (2009).
- ¹³M. Geiser, F. Castellano, G. Scalari, M. Beck, L. Nevou, and J. Faist, *Phys. Rev. Lett.* **108**, 106402 (2012).
- ¹⁴G. Scalari, C. Maissen, D. Turčinkova, D. Hagenmuller, S. De Liberato, C. Ciuti, C. Reichl, D. Schuh, W. Wegscheider, M. Beck, and J. Faist, *Science* **335**, 1323 (2012).
- ¹⁵O. Mitrofanov, C. C. Renaud, and A. J. Seeds, *Opt. Express* **20**, 6197 (2012).
- ¹⁶C. Maissen, G. Scalari, F. Valmorra, M. Beck, J. Faist, S. Cibella, R. Leoni, C. Reichl, C. Charpentier, and W. Wegscheider, *Phys. Rev. B* **90**, 205309 (2014).
- ¹⁷Y. Todorov, P. Desfonds, C. Belacel, L. Becerra, and C. Sirtori, *Opt. Express* **23**(13) 16838–16845 (2015).
- ¹⁸C. Feuillet-Palma, Y. Todorov, R. Steed, A. Vasanelli, G. Biasiol, L. Sorba, and C. Sirtori, *Opt. Express* **20**, 29121 (2012).
- ¹⁹A. Bhattacharya, G. Georgiou, S. Sawallich, C. Matheisen, M. Nagel, and J. Gomez Rivas, *Phys. Rev. B* **93**, 035438 (2016).
- ²⁰O. Mitrofanov, I. Brener, T. S. Luk, and J. L. Reno, *ACS Photonics* **2**, 1763 (2015).
- ²¹Z. Han, Y. Zhang, and S. I. Bozhevolnyi, *Opt. Lett.* **40**, 2533 (2015).
- ²²Y. Zhang and Z. Han, *Sci. Rep.* **5**, 18606 (2015).
- ²³I. Khromova, M. Navarro-Cía, I. Brener, J. L. Reno, A. Ponomarev, and O. Mitrofanov, *Appl. Phys. Lett.* **107**, 021102 (2015).
- ²⁴R. Mueckstein, C. Graham, C. C. Renaud, A. J. Seeds, J. A. Harrington, and O. Mitrofanov, *J. Infrared, Millimeter, Terahertz Waves* **32**, 1031 (2011).
- ²⁵O. Mitrofanov, I. Khromova, T. Siday, R. J. Thompson, A. N. Ponomarev, I. Brener, and J. L. Reno, *IEEE Trans. Terahertz Sci. Technol.* **6**, 382 (2016).
- ²⁶M. Natrella, O. Mitrofanov, R. Mueckstein, C. Graham, C. C. Renaud, and A. J. Seeds, *Opt. Express* **20**, 16023 (2012).
- ²⁷M. A. Kats, D. Woolf, R. Blanchard, N. Yu, and F. Capasso, *Opt. Express* **19**, 14860 (2011).
- ²⁸COMSOL Multiphysics, RF module.
- ²⁹L. Huang, D. R. Chowdhury, S. Ramani, M. T. Reiten, S.-N. Luo, A. K. Azad, A. J. Taylor, and H.-T. Chen, *Appl. Phys. Lett.* **101**, 101102 (2012).